Demonstration of Beat-to-Beat, On-Demand ATP Synthesis in Ventricular Myocytes Reveals Sex-Specific Mitochondrial and Cytosolic Dynamics

Paula Rhana, Collin Matsumoto, and L. Fernando Santana

Affiliation: Department of Physiology and Membrane Biology, School of Medicine, University of California, Davis, USA.

Running title: Per-Beat ATP Dynamics and Sex Differences in the Heart

Keywords: excitation-contraction coupling, excitation-metabolic coupling, mitochondria, oxidative phosphorylation.

Abstract

The substantial energetic demands on ventricular myocytes imposed by the transport of ions and cross-bridge cycling associated with each heartbeat are well known, yet the spatiotemporal dynamics of ATP supply and demand remain poorly understood. Here, using confocal microscopy and genetically encoded fluorescent sensors targeted to mitochondria and cytosol, we visualized beat-to-beat ATP dynamics in ventricular myocytes from adult male and female mice. These probes showed fluctuations in mitochondrial ATP levels with each contraction, revealing two distinct, spatially localized waveforms—ATP "gain" and ATP "dip"—representing transient increases or decreases in matrix ATP levels, respectively. These waveforms were tightly phase-locked to intracellular Ca^{2+} transients and organized into energetic microdomains. Although female myocytes exhibited larger local mitochondrial ATP transients than their male counterparts, their total mitochondrial volume was lower. Female myocytes also exhibited tighter coupling between the sarcoplasmic reticulum and mitochondria and showed a higher concentration of mitofusin 2 and ATP synthase catalytic α-subunit per unit volume, suggesting more efficient ATP production. Cytosolic ATP transients mirrored mitochondrial waveforms and domain structure in both male and female myocytes. During faster pacing, diastolic cytosolic ATP rose more rapidly in female myocytes, whereas the accompanying beat-locked ATP transients increased in both sexes but did so proportionally more in males than in females. These findings demonstrate that ATP is synthesized on demand—beat by beat—in a modular, microdomain-specific manner. We propose that male myocytes rely on greater mitochondrial mass for energetic scaling, whereas female cells employ architectural precision to optimize ATP delivery.

Key points summary

- It is known that each heartbeat requires precise ATP delivery to fuel ion transport and cross-bridge cycling, but the timing and spatial organization of ATP production in heart cells has been unclear.
- Using advanced imaging and genetically encoded sensors, we visualized beat-to-beat ATP fluctuations in the mitochondria and cytosol of individual male and female mouse ventricular myocytes.
- Mitochondrial ATP levels rose or fell with each beat in spatially confined regions, forming ATP "gain" or "dip" microdomains that were synchronized with Ca^{2+} transients.
- At higher firing rates, beat-locked, diastolic ATP transients rose more quickly in female myocytes, but were larger in male myocytes, highlighting distinct sex-specific strategies for matching energy supply to contractile demand.
- Ventricular myocytes "live paycheck-to-paycheck", producing just enough ATP on demand to fuel each beat. Male and female myocytes adopt distinct strategies to meet this demand: male myocytes scale output through greater mitochondrial mass, while female myocytes achieve energetic precision via enhanced sarcoplasmic reticulum–mitochondrial coupling.

First author profile

Paula Rhana, PhD, is an AHA Postdoctoral Fellow in Physiology & Membrane Biology, UC Davis. Trained in Biomedicine (BSc, FUMEC, Brazil) and Biochemistry & Immunology (MSc, PhD, UFMG, Brazil), Dr. Rhana discovered how voltage-gated Na^+ and Ca^{2+} channels drive breast tumor progression. Upon joining the Santana lab in 2022, she led the first effort to identify and characterize beat-to-beat mitochondrial ATP transients in adult cardiomyocytes using combined imaging and electrophysiological approaches. Her current research centers on mapping sex-specific metabolic microdomains that tune cardiac excitability, with the ultimate goal of translating these energetic insights and fluorescent-sensor innovations into new strategies for preventing and treating heart failure.

Introduction

The primary function of the heart is to pump blood through systemic and pulmonary circulations, delivering oxygen and nutrients to tissues and removing metabolic waste. To accomplish this, the heart contracts rhythmically—about 100,000 times per day in humans and 1 million times in mice—through a sequence of electrical and mechanical events known as the cardiac cycle. Each cycle begins with the generation of an action potential by pacemaker cells in the sinoatrial node and culminates in ventricular contraction and relaxation—tightly regulated processes that ensure adequate cardiac output under varying physiological demands.

The conversion of electrical excitation into mechanical force is mediated by a process termed excitation–contraction (EC) coupling (Eisner *et al.*, 2017). In ventricular myocytes, membrane depolarization triggers the opening of clusters of L-type Ca^{2+} channels ($Ca_V1.2$) in transverse tubules (Dixon *et al.*, 2012; Dixon *et al.*, 2015; Westhoff *et al.*, 2024; Spooner *et al.*, 2025), allowing a small influx of Ca^{2+} into the cytosol (Santana *et al.*, 1996; Wang *et al.*, 2001). This local Ca^{2+} signal activates ryanodine receptors in the adjacent junctional sarcoplasmic reticulum (SR) through a Ca^{2+}-induced Ca^{2+}-release mechanism (Fabiato, 1983). The resulting "Ca^{2+} sparks" raise intracellular (cytosolic) Ca^{2+} concentration ($[Ca^{2+}]_i$) and initiate actomyosin cross-bridge cycling and myocyte contraction (Cheng *et al.*, 1993; Cannell *et al.*, 1995; López-López *et al.*, 1995). This is followed by relaxation as Ca^{2+} is re-sequestered into the SR by the sarcoplasmic/endoplasmic reticulum Ca^{2+}-ATPase (SERCA) pump and extruded from the cell by the Na^+/Ca^{2+} exchanger, allowing the cycle to repeat (Balke *et al.*, 1994; Li *et al.*, 1998).

ATP fuels SERCA-driven Ca^{2+} reuptake, ion transport (via pumps and exchangers), and actomyosin cross-bridge cycling, with ~95% of this ATP supplied by mitochondrial oxidative metabolism and the remaining ~5% by glycolysis (Wisneski *et al.*, 1990; Saddik & Lopaschuk, 1991; Zhou & Tian, 2018; Lopaschuk *et al.*, 2021). Classic work has established coupling between Ca^{2+} handling and ATP production, showing that Ca^{2+} entering the mitochondrial matrix via the mitochondrial Ca^{2+} uniporter (MCU) activates three Ca^{2+}-sensitive dehydrogenases—pyruvate, isocitrate, and 2-oxoglutarate dehydrogenase; this boosts NADH production and drives proton flux through the ATP5A-containing F_1F_o-ATP synthase (Denton *et al.*, 1980; Denton & McCormack, 1990; McCormack *et al.*, 1990; Kirichok *et al.*, 2004; Garbincius & Elrod, 2022). Accordingly, in this process, mitochondrial efficiency is shaped not only by enzymatic capacity but also by organelle architecture and proximity to SR Ca^{2+}-release sites. The tethering protein mitofusin-2 (Mfn2), located on the outer mitochondrial membrane, mediate physical and functional coupling between mitochondria and the junctional SR, facilitating rapid Ca^{2+} transfer and enhancing oxidative phosphorylation (Chen *et al.*, 2012; Dorn *et al.*, 2015). Mitochondrial ATP production is supplemented by glycolysis and is further supported by creatine and adenylate kinase reactions, which draw on phosphocreatine and ADP pools to regenerate ATP. These pathways act in concert to maintain ATP supply across varying workloads. Despite the substantial energetic cost of each contraction cycle, prevailing models have assumed that intracellular ATP remains effectively constant due to the high throughput of mitochondrial ATP production, the rapid kinetics of phosphotransfer reactions, and the supplementary contribution of glycolysis (Chen *et al.*, 1998; Murphy & Steenbergen, 2008).

High-resolution imaging of intracellular ATP concentration ($[ATP]_i$) in beating ventricular myocytes has now upended this view. In Rhana *et al.* (2024), we showed that cytosolic ATP fluctuates with each ventricular beat and that these oscillations disappear when oxidative phosphorylation is inhibited, revealing the limited buffering capacity of phosphotransfer and the dominant role of mitochondria in sustaining EC coupling. These findings raise two questions that are addressed in the present study: (i) How tightly are SR Ca^{2+} release and mitochondrial ATP synthesis temporally linked during each beat? And (ii), given emerging evidence for sex-specific differences in

mitochondrial content and function (Cao et al., 2022), how do the kinetics and amplitudes of cytosolic and mitochondrial ATP transients differ between male and female cardiomyocytes?

In this study, we address these questions by directly monitoring cytosolic and mitochondrial ATP dynamics in beating male and female ventricular myocytes using newly developed expressible indicators, revealing a previously unrecognized, modular and beat-synchronized mode of ATP production. By comparing mitochondrial and cytosolic ATP fluctuations within the same cell type under physiological pacing conditions, we test the hypothesis that mitochondrial ATP, like its cytosolic counterpart, varies beat to beat in response to EC coupling. Building on evidence that mitochondrial volume, gene expression, and SR–mitochondrial coupling differ between male and female hearts (Cao *et al.*, 2022; Clements *et al.*, 2023), we further examine how stimulation frequency and biological sex shape these dynamics.

Our results reveal that cytosolic and mitochondrial ATP oscillate in synchrony with the cardiac cycle and show that these oscillations are modulated by stimulation frequency and differ according to sex. Female myocytes exhibit a faster rise in diastolic cytosolic ATP during increased pacing that coincides with stronger SR–mitochondrial coupling and higher expression of Mfn2 and ATP5A. In contrast, mitochondrial volume is greater in male myocytes, and the amplitude of beat-to-beat ATP transients in these cells is selectively increased under load. Together, these findings support a model in which mitochondria participate dynamically in the beat-to-beat regulation of cardiac energetics and suggest sex-specific strategies—mass-based scaling versus architectural precision—for matching energy supply to contractile demand.

Methods and Materials

Ethical approval. This study adhered to the guidelines set forth in the National Institutes of Health (NIH) Guide for the Care and Use of Laboratory Animals. The Institutional Animal Use and Care Committee (IACUC) at the University of California, Davis, approved our animal use and protocols, which align with ARRIVE guidelines.

Infection of mice with adeno-associated viruses (AAVs). Male and female C57BL/6J mice (8–12 weeks old) were used for all experiments. Adeno-associated virus serotype 9 (AAV9) particles carrying either the cytosolic iATP reporter iATPSnFR$^{1.0}$ (Lobas *et al.*, 2019) or the mitochondria-targeted reporter iATPSnFR$^{2.0}$ (Marvin *et al.*, 2024), here termed cyto-iATP and mito-iATP, respectively, were prepared at 4 x 10^{12} viral genome copies per milliliter (vg/mL). Mice were anesthetized with 5% isoflurane and maintained at 2% isoflurane, with concurrent administration of 100 µL of viral suspension via retro-orbital injection using a microsyringe.

Isolation of mouse ventricular myocytes. Mice were euthanized 1–2 weeks post AAV infection by intraperitoneal injection of a lethal dose of pentobarbital (100 mg/kg). Each heart was rapidly excised, its aorta was cannulated, and the preparation was perfused on a constant-flow Langendorff apparatus using an enzymatic solution for cardiomyocytes isolation, as previously described (Shioya, 2007; Rossow *et al.*, 2009). Isolated ventricular myocytes were maintained at room temperature (~24°C) in Tyrode's solution (130 mM NaCl, 5.4 mM KCl, 1.8 mM $CaCl_2$, 0.33 mM NaH_2PO_4, 25 mM HEPES, 22 mM glucose, and 0.5 mM $MgCl_2$, pH 7.4, adjusted using NaOH) and used within 5 hours of isolation.

Field stimulation. Action potentials were evoked by field stimulation using two platinum wires separated by 0.5 cm, positioned at the bottom of the perfusion chamber. Square, 4-ms voltage pulses were generated using a Grass stimulator (AstroMed Inc., USA). Pulses (amplitudes, 10–40 V) were delivered at frequencies ranging from 0.5 to 3.0 Hz.

Confocal imaging of action potential-evoked $[Ca^{2+}]_i$, $[ATP]_i$, and $[ATP]_{mito}$ signals. Cytosolic Ca^{2+} was imaged by loading ventricular cardiomyocytes expressing the cyto-iATP or mito-iATP sensor with 10 µM Rhod-3-AM (Thermo Fisher, USA) following manufacturer's guidelines. After loading with Rhod-3, a drop of the cell suspension was transferred to a temperature-controlled (37°C) perfusion chamber on a microscope stage and allowed to settle onto the coverslip for 5 minutes. Cells were then perfused with Tyrode's solution and field stimulated. Diastolic and systolic $[Ca^{2+}]_i$ and $[ATP]_i$ or $[ATP]_{mito}$ signals were simultaneously recorded using an inverted Olympus FV3000 confocal microscope (Olympus, Japan) operating in 2D or line-scan mode. Fluorescent indicators were excited with solid-state lasers emitting at 488 nm (cyto-iATP and mito-iATP) or 561 nm (Rhod-3) through a 60× oil-immersion lens (PlanApo) with a numerical aperture (NA) of 1.40. During analysis, background was subtracted from all confocal images, and fluorescence signals were expressed as F/F_0, where F is the fluorescence intensity at a given time point and F_0 is the mean baseline fluorescence. Cyto-iATP fluorescence values were converted to concentration units using the pseudo-ratiometric method (Cheng *et al.*, 1993). A dissociation constant (K_d) of 1460 µM and a resting level of $[ATP]_i$ of 457 µM was used in these calculations (Rhana *et al.*, 2024).

Super-resolution radial fluctuation (SRRF) imaging. Freshly isolated ventricular myocytes expressing cyto-iATP or mito-iATP sensors were incubated for 30 minutes at 37°C with 250 nM MitoTracker Deep Red (Molecular Probes, USA). SRRF images were acquired using Fusion software on an Andor Dragonfly 200 spinning-disk confocal platform (Andor Technologies, UK) coupled to an inverted Leica DMi* microscope fitted with a 60× oil-immersion objective (NA =

1.40) and Andor iXon EMCCD camera. Colocalization analyses for mito-iATP versus MitoTracker and cyto-iATP versus MitoTracker were performed using IMARIS software.

Mitochondrial volume analysis. Ventricular myocytes from male and female mice were incubated with 250 nM MitoTracker Deep Red (Thermo Fisher Scientific) for 30 minutes at 37°C. Cells were allowed to adhere to poly-L-lysine/laminin-coated coverslips for 1 hour at room temperature, then fixed with 4% formaldehyde diluted in phosphate-buffered saline (PBS; Fisher Scientific, USA) for 15 minutes. Coverslips were mounted using Vectashield mounting medium (Vector Laboratories, USA) and sealed with clear nail polish. Confocal z-stacks were acquired on an Olympus FV3000 confocal microscope using a 60× oil-immersion objective (NA = 1.40), with a z-step of 0.5 µm. After importing three-dimensional (3D) image stacks into IMARIS 10 (Andor, UK), mitochondria were segmented based on MitoTracker fluorescence intensity using the Surfaces tool and a consistent thresholding approach. Total mitochondrial volume was quantified for each cell and normalized to cytosolic volume to obtain the mitochondrial volume fraction.

Western blots. Female and male ventricles were collected and homogenized in ice-cold RIPA buffer supplemented with a cocktail of protease inhibitors (Pierce Protease Inhibitor Mini Tablets; Thermo Scientific, USA). Proteins (80 µg) were separated by sodium dodecyl sulfate-polyacrylamide gel electrophoresis (SDS-PAGE) followed by semi-dry transfer onto a PVDF (polyvinylidene fluoride) membrane. Membranes were washed in Tris-buffered saline containing 0.1% Tween-20 (TBS-T), blocked in TBS-T containing 5% bovine serum albumin (BSA) for 1 hour at room temperature, and incubated overnight at 4°C with anti-Mfn2 (1:1000, #9482S; Cell Signaling, USA) and anti-ATP5A1 (1:1000, #459240; Invitrogen, USA), prepared in TBS-T containing 5% BSA. Membranes were then rinsed with TBS-T and incubated with mouse IgG 800CW or rabbit IgG 680CW secondary antibodies (1:15,000; Li-Cor, USA) for 1 hour at room temperature. Fluorescence signals were detected using an Odyssey Infrared Imager (LiCor, USA). Blots were digitized and bands quantified using ImageJ. Protein levels were expressed as the ratio of optical densities of specific bands to total protein levels.

Statistics. Data are presented as means ± standard error of the mean (SEM). Normality was assessed for all data sets. Group comparisons were performed using Student's *t*-test or analysis of variance (ANOVA) followed by a multiple comparison test. Statistical significance was defined as $P < 0.05$, with individual significance values indicated in figure legends as follows: $P < 0.05$ (*), $P < 0.01$ (**), $P < 0.001$ (***), and $P < 0.0001$ (****).

Results

Mitochondrial ATP transients exhibit two beat-locked waveforms with a sex-dependent spatial distribution

Mitochondrial ATP was imaged using a mitochondrial matrix-targeted intracellular ATP (iATP) sensor termed mito-iATP, a version of the low-affinity A95A/A119L variant (apparent $K_d \approx 0.5$ mM) of the high-dynamic-range reporter, iATPSnFR2, created by fusing four tandem COX8 leader sequences to the N-terminus of iATPSnFR2 and cloning it into an AAV9 cassette, as described by Marvin *et al.* (2024). Wide-field confocal imaging performed on adult mouse ventricular myocytes expressing mito-iATP (**Figure 1A**) showed that mito-iATP fluorescence formed a finely striated reticulum that colocalized with MitoTracker Deep Red, with no detectable cytosolic signal in either male or female myocytes. A magnified 10 x 10 µm view (**Figure 1A insets)** illustrates the pixel-level concordance between the two channels. A quantitative colocalization analysis yielded Manders' coefficients of 0.94 ± 0.01 for female and 0.99 ± 0.01 for male myocytes, indicating precise targeting throughout the mitochondrial lattice. As shown in **Figure 1B**, brief bath application of 1 µM FCCP, an uncoupler of oxidative phosphorylation, decreased mito-iATP fluorescence from a normalized F/F_0 value of 1.0 to 0.68 ± 0.05 ($P < 0.0001$), demonstrating that mito-iATP reliably reports dynamic changes in matrix ATP concentration.

To test whether $[ATP]_{mito}$ fluctuates on a beat-to-beat basis, we loaded myocytes expressing mito-iATP with the red-shifted Ca^{2+} indicator Rhod-3 and applied field stimulation at 1 Hz. Representative line-scan images (**Figure 2A, B**) captured simultaneous $[Ca^{2+}]_i$ (upper trace) and matrix ATP (lower trace) responses during individual action potentials. Each stimulus elicited a phasic $[ATP]_{mito}$ fluctuation that was tightly phase-locked to the $[Ca^{2+}]_i$ transient. Two reproducible waveform types were identified. In the first (Mode 1), $[ATP]_{mito}$ rose rapidly and then returned to baseline (**Figure 2A**). In the second (Mode 2), $[ATP]_{mito}$ dipped transiently and recovered with similar kinetics (**Figure 2B**). These opposite-polarity responses coexisted within single myocytes, but were spatially segregated, revealing a patchwork of energetic microdomains. Importantly, the amplitude of whole-cell $[Ca^{2+}]_i$ transients was similar in cells displaying either Mode 1 or Mode 2 fluctuations across both sexes (**Figure 2C**) (2.40 ± 0.10 and 2.59 ± 0.14 F/F_0 for Mode 1 and Mode 2 sites, respectively, in females, and 2.26 ± 0.15 and 2.58 ± 0.28 F/F_0 for Mode 1 and Mode 2 sites in males). The average $[ATP]_{mito}$ amplitudes of Mode 1 sites (1.53 ± 0.05 F/F_0 in females and 1.47 ± 0.04 F/F_0 in males) and Mode 2 sites (0.71 ± 0.02 F/F_0 in females and 0.70 ± 0.02 F/F_0 in males) were similar across sexes (**Figure 2D**).

Quantification of over 30 individual mito-iATP sites revealed a modest, but consistent, sex difference in waveform prevalence. In females, 43% of cells exhibited Mode 1 exclusively, 7% exhibited Mode 2 exclusively, and 50% showed both modes; in males, the corresponding proportions were 38%, 8%, and 54%. Despite this difference in spatial distribution, the average length of local transients was indistinguishable between sexes: Mode 1 sites averaged around 25 µm (25 ± 2 µm in females and 26 ± 2 µm in males), whereas Mode 2 sites averaged 18 ± 2 µm in both sexes (**Figure 2E**). Given that a single mitochondrion spans ~1.5–2 µm, these measurements suggest that each narrow line-scan region captures synchronous ATP fluctuations across strings of adjacent ~10–18 interfibrillar mitochondria (Moreland, 1962; Hom & Sheu, 2009), confirming the microdomain nature of these events.

Despite comparable amplitudes, the spatial patterning of $[ATP]_{mito}$ elevations along interfibrillar mitochondrial strings was more heterogeneous in females (**Figure 2F**). To quantify this, we calculated the coefficient of variation (CV = standard deviation/mean) of mito-iATP signals along the transient peak. The CV was significantly greater in female (0.14 ± 0.01) than male (0.09 ± 0.01) myocytes ($P < 0.01$) (**Figure 2G**), suggesting greater spatial variability in mitochondrial ATP

synthesis. Consistent with this, ATP "hotspots" in cardiomyocytes reached higher peak values in females (1.84 ± 0.11 F/F_0) than males (1.49 ± 0.05 F/F_0; $P < 0.01$), even though the average amplitude per site remained equivalent (**Figure 2H**).

To assess sex-dependent differences in the kinetics of mitochondrial ATP transients, we quantified time-to-peak and time-to-decay for Mode 1 and Mode 2 responses (**Figure 3A, B**). In Mode 1 sites, $[ATP]_{mito}$ rose faster in females (80 ± 4 ms) than in males (97 ± 5 ms; $P < 0.01$), while Mode 2 rise times were similar between sexes (females: 107 ± 11 ms; males: 106 ± 11 ms) (**Figure 3C**). Time to 90% decay was also comparable across sex and mode (**Figure 3D**) (females, 123 ± 10 and 144 ± 17 ms for Mode and Mode 2 sites, respectively; males, 135 ± 12 and 121 ± 16 ms for Mode and Mode 2 sites). The time-to-peak and time-to-decay values for $[Ca^{2+}]_i$ transients were similar in Mode 1 and Mode 2 sites across both sexes (**Figure 3E,F**). It is important to note that, while $[Ca^{2+}]_i$ and $[ATP]_{mito}$ transients are shown for temporal alignment, a direct comparison of their kinetics should be interpreted with caution, given the markedly faster response properties of Rhod-3 compared with those of the EGFP-based mito-iATP sensor.

Together, these findings demonstrate that millisecond-scale ATP transients can be visualized within adult ventricular mitochondria and that they adopt two discrete, spatially confined waveforms. While peak amplitudes are similar, the relative distribution, spatial heterogeneity, and kinetics of these events differ between male and female myocytes, raising the possibility that sex-specific energetic strategies reflect both mitochondrial abundance and subcellular organization.

Despite a lower mitochondrial volume, female myocytes display a higher mitochondrial density of Mfn2 and ATP5A

We postulated that the smaller local ATP signals and lower prevalence of ATP-gain microdomains observed in male myocytes might stem from sex differences in both mitochondrial content and the spatial relationship between mitochondria and sites of SR Ca^{2+} release. Voxel segmentation of 3D confocal image stacks from Mitotracker-labeled ventricular myocytes revealed that mitochondria occupied 6391 ± 310 μm^3 of cytosolic volume in females versus 8192 ± 231 μm^3 in males (n = 30 cells per sex; $P < 0.0001$) (**Figure 4A, B**).

To explore the molecular correlates of this architectural divergence, we quantified the expression of Mfn2, a key tethering protein that links mitochondria to the SR and facilitates Ca^{2+}-dependent stimulation of oxidative phosphorylation (Chen *et al.*, 2012; Dorn *et al.*, 2015; Rhana *et al.*, 2024), and ATP5A, a core subunit of the mitochondrial ATP synthase complex. These proteins were selected for evaluation because of their roles in inter-organelle coupling (Mfn2) and bioenergetic output capacity (ATP5A). Immunoblotting showed that bulk levels of ATP5A and Mfn2 were similar between sexes (**Figure 4C–E**).

Given our observation that mitochondrial volume is lower in female than male myocytes, the similar expression levels of Mfn2 and ATP5A suggest a higher mitochondrial density of these proteins in female myocytes. This enrichment aligns with our imaging data showing the emergence of discrete mito-iATP hotspots—transient, spatially confined increases in mitochondrial ATP—throughout the matrix of female, but not male, myocytes. We propose that the combination of tighter SR–mitochondrial tethering and higher bioenergetic protein density enhances the spatial precision and temporal responsiveness of oxidative phosphorylation in female myocytes, promoting local ATP surges in regions of Ca^{2+} flux during EC coupling.

Cytosolic ATP transients mirror mitochondrial waveforms and exhibit a sex-dependent domain organization

To assess cytosolic ATP dynamics, we used iATPSnFR1—the original genetically encoded fluorescent ATP sensor developed by Lobas *et al.* (2019) that lacks organelle-targeting sequences and distributes freely throughout the cytoplasm. The construct, here termed cyto-iATP,

was packaged into an AAV9 vector and expressed in adult ventricular myocytes from male and female mice. Confocal imaging showed a uniform, diffuse fluorescence pattern throughout the cytosol in male or female myocytes, with no detectable signal in mitochondria (**Figure 5**). Co-staining with Mitotracker Deep Red confirmed that cyto-iATP was excluded from the mitochondrial compartment, with merged images revealing clear separation between the two signals in both male and female cells, validating the specificity of cytosolic expression (Mander's correlation coefficients: 0.68 ± 0.02 and 0.57 ± 0.02 in female and male myocytes, respectively). Magnified 10 x 10 μm regions illustrate the lack of overlap at high resolution, providing assurance that the probe selectively reports cytosolic ATP concentration ($[ATP]_i$) without mitochondrial contamination.

To determine whether $[ATP]_i$ exhibits beat-to-beat fluctuations during EC coupling, we recorded simultaneous line-scan images of cyto-iATP and Rhod-3 fluorescence in cells subject to field stimulation (1 Hz). As with mitochondrial ATP, $[ATP]_i$ underwent rhythmic phasic changes that were tightly phase-locked to the $[Ca^{2+}]_i$ transient (**Figure 6**). Two distinct waveform types—Mode 1 and Mode 2—were identified. In Mode 1 (**Figure 6A**), $[ATP]_i$ rose rapidly after the Ca^{2+} transient and returned to baseline before the next beat. In Mode 2 (**Figure 6B**), $[ATP]_i$ dipped transiently and recovered with similar timing. Both modes were present within single cells and segregated spatially, revealing a cytosolic energetic microdomain structure analogous to that observed in the mitochondrial matrix.

Quantification of local and global $[ATP]_i$ and $[Ca^{2+}]_i$ transients revealed striking parallels to the mitochondrial data (**Figure 6C–F**). Mode 1 and Mode 2 events were detected in myocytes of both sexes, and their spatial distribution followed a similar sex-dependent pattern: female myocytes exhibited a higher proportion of ATP-gain (Mode 1) domains (58% in females and 40% in males), whereas male myocytes had more ATP-dip (Mode 2) regions (10% in females and 13% in males). Local transient amplitudes did not differ significantly between sexes for either mode (1.25 ± 0.02 and 0.77 ± 0.02 F/F_0 for Mode 1 and Mode 2 sites in females, and 1.27 ± 0.03 and 0.79 ± 0.02 F/F_0 for Mode 1 and Mode 2 sites in males), indicating that the intrinsic dynamics of each waveform are comparable. However, global F/F_0 signals were significantly larger in male than female myocytes for both Mode 1 (1.10 ± 0.01 F/F_0 vs 1.12 ± 0.01 F/F_0; $P < 0.05$) and Mode 2 (0.96 ± 0.01 F/F_0 vs 0.91 ± 0.01 F/F_0; $P < 0.05$)(**Figure 6C,D**), consistent with a greater fraction of the cytosol participating in each mode in male cells. Thus, the amplitude of $[Ca^{2+}]_i$ transients was similar in cells displaying either Mode 1 or Mode 2 fluctuations across both sexes (**Figure 6E, F**).

To evaluate sex- and mode-dependent differences in the kinetics of $[ATP]_i$ transients, we measured the time to peak and decay in Mode 1 and Mode 2 regions of male and female myocytes (**Figure 7A,B**). Unlike $[ATP]_{mito}$ transients, $[ATP]_i$ transients in Mode 1 sites showed no significant difference in the time to 90% peak between sexes (87 ± 6 ms for both) (**Figure 7C**). However, time to 90% peak $[ATP]_i$ at Mode 2 sites differed between female (75 ± 5 ms) and male (107 ± 11 ms) myocytes ($P < 0.05$). As was the case for $[ATP]_{mito}$ transients, we observed no difference in time-to-decay of $[ATP]_i$ transients across sexes and modes or the kinetics of whole-cell $[Ca^{2+}]_i$ transients (**Figure 7D–F**).

Together, these findings demonstrate that cytosolic ATP, like mitochondrial ATP, fluctuates on a beat-to-beat basis in two distinct modes, and that the sex-dependent differences in global amplitude arise from variations in the spatial distribution of these energetic domains rather than from differences in ATP waveform magnitude or Ca^{2+} signaling.

Increasing workload elevates $[ATP]_i$ more rapidly and to a greater extent in male than female myocytes

To determine whether the ~20% lower mitochondrial volume in female ventricular myocytes slows cytosolic ATP replenishment during increased workload, we monitored diastolic $[ATP]_i$ in cells paced at varying frequencies (**Figure 8**). Upon switching from quiescence (0 Hz) to 2-Hz stimulation, diastolic $[ATP]_i$ rose and stabilized at a higher set point that persisted throughout pacing (**Figure 8A–C**). The new diastolic $[ATP]_i$ values (in F/F_0 units) were 1.22 ± 0.03 in female and 1.25 ± 0.02 in male myocytes (**Figure 8D**). Notably, further increasing pacing to 3 Hz produced no additional rise ($p = 0.96$), suggesting a physiological ceiling to workload-induced ATP enhancement.

Because the relationship between actual $[ATP]_i$ and cyto-iATP fluorescence is nonlinear, we converted these F/F_0 values to estimated ATP concentrations, assuming a basal diastolic $[ATP]_i$ of 457 μM (Lobas *et al.*, 2019; Rhana *et al.*, 2024). Although the 2 Hz-evoked mean diastolic $[ATP]_i$ trended lower in female (608 ± 17 μM) than male (636 ± 18 μM) myocytes, this difference was not statistically significant ($p = 0.14$), indicating comparable resting ATP levels between sexes (**Figure 8E**).

We then fit the time course of the diastolic $[ATP]_i$ rise (in μM) using a single-exponential function. Kinetic fits were applied to the estimated $[ATP]_i$ rather than F/F_0 to avoid nonlinearity-induced distortions in estimating time constants. This analysis revealed that female myocytes reached their new steady-state ATP level with a time constant (τ) of 3.66 ± 0.18 minutes, whereas male myocytes required ~23% longer (τ = 4.50 ± 0.29 minutes; $P < 0.01$) (**Figure 8F**). This sex difference supports the hypothesis that tighter SR–mitochondrial coupling in female myocytes enables more rapid activation of oxidative phosphorylation, while weaker coupling in male myocytes introduces a delay.

Together, these data suggest that the diastolic component of the cytosolic ATP response to increased workload is governed by intrinsic kinetic programs modulated by both mitochondrial reserve and SR–mitochondrial coupling. Female myocytes achieve faster ATP upregulation despite reduced mitochondrial content, whereas male myocytes rely on greater mitochondrial mass but exhibit slower metabolic adaptation.

Differential modulation of beat-to-beat $[ATP]_i$ transients by pacing frequency in male and female myocytes

To test how acute workload modulates cytosolic ATP oscillations, we imaged cyto-iATP signals in ventricular myocytes paced first at 1 Hz and then at 2 Hz (**Figure 9**). We selected 2 Hz because diastolic $[ATP]_i$ rises in response to this—but not higher—frequencies, as mentioned in **Figure 8**, making it the highest rate that reliably elevates energetic demand while preserving cellular integrity. Because diastolic $[ATP]_i$ is higher at 2 Hz, beat-evoked F/F_0 values were converted to concentration units using sex-specific baselines (male, 638 μM; female, 608 μM).

At 1 Hz, beat-to-beat $[ATP]_i$ elevations (Mode 1) were comparable in female and male cells. Pacing at 2 Hz increased the amplitude of these gains in both sexes (females, 555 ± 10 μM → 718 ± 14 μM; males, 587 ± 15 μM → 811 ± 28 μM; each $P < 0.0001$), with males showing the larger absolute rise ($P < 0.05$). Expressed as $\Delta[ATP]_i$, values in male myocytes again exceeded those in female myocytes at both 1 Hz (130 ± 15 μM vs. 98 ± 10 μM) and 2 Hz (173 ± 28 μM vs. 111 ± 14 μM; $P < 0.05$).

Mode 2 regions, which exhibit ATP dips, behaved similarly at 1 Hz in both sexes. Raising the rate to 2 Hz shifted the dips to higher absolute concentrations (females, 380 ± 17 μM → 542 ± 24 μM; males, 383 ± 12 μM → 464 ± 18 μM; each $P < 0.001$), yet the depth of the dip ($\Delta[ATP]_i$) became markedly larger in males (−174 ± 18 μM) than in females (−66 ± 24 μM; $P < 0.0001$).

Taken together with our evidence of greater mitochondrial volume in males and tighter SR–mitochondrial coupling in females, these data support a model in which female myocytes meet heightened demand through architectural precision and efficient local production, whereas male myocytes rely on a mass-based scaling strategy that permits larger beat-coupled ATP swings but may approach capacity sooner. Thus, beat-synchronized ATP synthesis is modular and plastic, and its quantitative tuning differs between male and female cardiomyocytes.

Discussion

In the current study, we demonstrate that ATP is not continuously produced in adult ventricular myocytes but instead is generated in a beat-to-beat fashion through an on-demand process that is tightly coupled to EC coupling. Using a matrix-targeted, low-affinity variant of iATPSnFR, mito-iATPSnFR2 (here termed mito-iATP), we were able to visualize rhythmic mitochondrial ATP transients with millisecond precision and show that they were phase-locked to each action potential and propagated to the cytosol. These transients showed differences in relative prevalence, but not amplitude, between male and female cardiomyocytes, and appeared as spatially confined micro-domains—some showing ATP gains, others ATP dips. Thus, ATP supply is organized into discrete, temporally synchronized bursts that match the periodicity of cellular demand. In this view, ventricular myocytes "live paycheck-to-paycheck", producing just enough ATP during each beat to fuel contraction.

By imaging ATP within the mitochondrial matrix, we extend our prior findings of cytosolic ATP oscillations during EC coupling (Rhana *et al.*, 2024) and identify their origin as upstream pulses of mitochondrial ATP production. The coexistence of gain and dip domains within the same cell, together with their regional segregation, underscore the spatially modular aspect of mitochondrial output in addition to its phasic quality. While female myocytes exhibit a higher fraction of ATP-gain regions and male cells show more dip domains, local $[ATP]_i$ transient amplitudes are conserved, indicating that the observed sex differences reflect spatial distribution rather than intrinsic mitochondrial capacity.

An interesting observation in this study is that mito-iATP signals—presumably arising from intrafibrillar mitochondrial strings—extend over comparable distances in male and female ventricular myocytes (~30 μm), suggesting that each string houses roughly the same number of individual mitochondria (~15–20, assuming a length of 1.5–2.0 μm in adult cells). Yet, because female myocytes possess a smaller overall mitochondrial volume, they must harbor fewer such strings per cell. Superimposed on this reduced network is a higher density of both the tethering protein Mfn2 and the catalytic α-subunit of the F_1F_o-ATP-synthase, ATP5A, per mitochondrion in female myocytes. This dual enrichment provides two complementary advantages. First, an elevated Mfn2-to-mitochondrion ratio tightens SR–mitochondrial coupling, sharpening Ca^{2+} microdomains around select organelles. Second, greater ATP5A content boosts the local catalytic capacity of ATP synthase, enabling these Ca^{2+}-favored mitochondria to more effectively transduce proton motive force into ATP. Together, these features likely underpin the pronounced "hot spots" of ATP synthesis detected in female cells—zones where Ca^{2+} delivery and ATP-synthase density coincide—as well as the relatively quiescent neighboring regions, where there are fewer tethers and lower ATP5A. In contrast, male myocytes achieve more spatially homogeneous rises in $[ATP]_{mito}$ by distributing a larger overall mitochondrial mass with lower per-mitochondrion ATP5A, relying on quantity rather than precision for energetic scaling. Ultrastructural evidence of denser cristae and heightened Ca^{2+} responsiveness in female cardiomyocyte mitochondria reinforces the idea that architectural precision, coupled with enhanced catalytic machinery, allows female myocytes to meet localized energy demands efficiently. This sex-specific balance between mitochondrial abundance and per-organelle capacity may help explain the greater resistance of female hearts to acute energetic stress and offers a framework for understanding how subtle shifts in protein density can reshape cellular bioenergetic landscapes.

Consistent with this microdomain view, recent systems-genetics work by Cao *et al.* (2022) uncovered a sex-biased gradient in global mitochondrial supply and performance. This previous study reported that, across >100 inbred mouse strains and two independent human heart cohorts, female ventricles carry ~10–20% fewer mitochondrial genomes and display coordinated down-regulation of both nuclear- and mtDNA-encoded oxidative-phosphorylation transcripts. From a

functional standpoint, this study showed that mitochondria isolated from female hearts exhibit markedly lower state-3 and maximal respiration and reduced complex II/IV flux. Using gonadectomy plus hormone-replacement experiments, it also revealed that mitochondrial biogenesis is controlled by an androgen-supported, estrogen-restrained process. This study further demonstrated that strain-level correlations link higher mtDNA and respiratory capacity to superior diastolic indices, and that overexpression of the male-biased fatty-acyl–CoA ligase, ACSL6, improves both mitochondrial function and lusitropy, especially in female myocytes. Thus, female hearts rely on a lean, precisely deployed reserve that suffices at rest yet may falter under increased workloads, whereas male hearts buffer demand with greater mitochondrial mass.

This architectural divergence has functional implications under stress. Imaging of mitochondrial and cytosolic ATP showed that mitochondrial ATP output reaches the cytosol within one beat and retains the same microdomain pattern. Raising pacing from 1 to 2 Hz increased Mode 1 (ATP-gain) amplitudes in both sexes, but the absolute rise was larger in males. At baseline, the gains were indistinguishable, indicating that the difference emerges only under higher workload. In Mode 2 (ATP-dip) regions, the troughs shifted to higher absolute $[ATP]_i$ in both; however, the depth of the dip became markedly greater in male myocytes while exhibiting a smaller negative excursion in female myocytes. These findings suggest that male myocytes meet the added demand primarily by drawing on their larger mitochondrial pool, which allows larger beat-coupled swings in ATP but also leaves less net gain once consumption rises. Female myocytes, with tighter SR–mitochondrial coupling, limit the depth of the dips and maintain gain amplitudes, pointing to efficient local production that matches consumption within each microdomain. Thus, myocytes of both sexes accommodate increased workload, but male myocytes do so by scaling flux through greater mitochondrial mass, whereas female myocytes rely on architectural precision to sustain ATP levels beat by beat.

A temporal analysis revealed additional sex-specific distinctions in ATP regulation. Most female myocytes reestablished diastolic ATP levels within ~3.7 minutes, consistent with rapid oxidative mobilization and tighter local control via SR–mitochondrial coupling. In contrast, male myocytes exhibited a slower (~4.5 minutes) but stable increase, aligning with a strategy based on greater mitochondrial mass but weaker coupling. We interpret the fast kinetic phase as activation of pre-engaged mitochondrial domains already operating near maximal dehydrogenase activity, and the slower phase as reflecting recruitment of latent domains requiring Ca^{2+}-driven NADH buildup. The dominance of the fast phase in female myocytes may reflect a strategic trade-off: fewer, more efficiently wired mitochondria enable rapid initiation but may limit the scalability of sustained energetic adaptation. This interpretation refines the classical concept of mitochondrial reserve capacity (Bertero & Maack, 2018) by linking it to spatial architecture and provides a mechanistic link between structural sex differences (Cao *et al.*, 2022) and functional disparities in ATP dynamics.

Importantly, our findings reframe cardiac energetics as modular and dynamic. Rather than forming a homogeneous ATP pool, mitochondrial output is organized into spatially restricted domains that deliver ATP in synchrony with each heartbeat. This modularity offers local control over supply and demand, buffering ATP-consuming processes such as ion transport and contraction. Biological sex modulates this topology through differences in mitochondrial abundance and organization, shaping how the heart adapts to stress and matches energy supply with demand.

These principles echo those observed in neurons, where mitochondria positioned near synapses supply ATP to match local firing demand (Rangaraju *et al.*, 2014). The situation is similar in sinoatrial node pacemaker cells (Yaniv *et al.*, 2013). Although the assays used in this study were unable to resolve individual beat-to-beat changes, they showed that supply and demand were matched on a seconds-to-minutes timescale, reflecting a boost in ATP production due to recruitment of mitochondrial Ca^{2+} uptake and cAMP/protein kinase A signaling in response to

increases in spontaneous firing rate. Taken together, these observations across neurons, pacemaker cells, and ventricular myocytes reinforce the view that a spatially and temporally modular ATP-delivery process is a conserved strategy for sustaining the function of excitable cells.

Although we did not calibrate absolute matrix [ATP], the robust mito-iATP oscillations raise important questions about mitochondrial ATP levels. Assuming an apparent K_d for iATPSnFR2 of ~0.5 mM (Marvin *et al.*, 2024), the clear fluorescence changes observed suggest free mitochondrial [ATP] may be closer to 1–5 mM than the ~7.5 mM value estimated based on biochemical approaches (Schwenke *et al.*, 1981). Considered together with $[ATP]_i$ < 1 mM (Rhana *et al.*, 2024), this gives rise to a paradox: if neither compartment contains high ATP concentrations, where is the ~8 mM total cellular ATP measured by NMR (Eisner & Murphy, 2024)? This discrepancy likely reflects the fact that most cellular ATP exists in bound forms (e.g., protein-associated) or in compartments invisible to fluorescent sensors, which detect only free ATP. This revised view—with low free ATP in both compartments—explains why inhibiting oxidative phosphorylation does not increase cytosolic ATP as predicted by previous studies (Eisner & Murphy, 2024). Instead of relying on large static pools, the operation of the cardiac ATP-production process appears to be defined by rapid, localized production within microdomains, with most cellular ATP sequestered in bound forms that buffer against depletion while enabling dynamic local signaling. Future studies should address this intriguing question.

Our findings also underscore the critical dependence of cardiac energetics on uninterrupted blood flow and functional hyperemia (Feigl, 1983; Manning *et al.*, 2024). The rapid, beat-synchronized nature of mitochondrial ATP synthesis suggests that energy supply in the heart is dynamically scaled to immediate demand with minimal reserve capacity. This temporal precision implies that continued delivery of oxygen and metabolic substrates through the coronary circulation is essential not just for long-term metabolic health, but for the energetic integrity of each individual heartbeat. Disruptions in blood flow—whether transient or sustained—could compromise the mitochondrial response to $[Ca^{2+}]_i$ transients, thereby affecting contractile performance and electrical stability within just a few cardiac cycles. Our findings therefore reinforce the view that perfusion and metabolism are moment-to-moment co-regulators of cardiac function.

In summary, ATP supply in adult ventricular myocytes is shaped by a network of beat-coupled, spatially organized production units. Mitochondria discharge ATP in phasic bursts that are aligned with each action potential and propagate to the cytosol to support rhythmic contractile demands. Sex-specific differences in mitochondrial mass and SR coupling further tune this architecture, with male myocytes leveraging volume for output and female myocytes achieving stability through precision. These findings compel a revision of traditional bioenergetic models and suggest that cardiac metabolic resilience is governed as much by spatial design as by absolute capacity.

Data availability statement

The raw data files supporting all findings presented in this paper are available from the corresponding author.

Competing interests

The authors declare that they have no competing interests.

Author contributions

PR and LFS conceived and designed the work. PR and CM acquired and analyzed data for the paper. PR, CM, and LFS wrote the paper. All authors have approved the final version of the manuscript and agreed to be accountable for all aspects of the work. All persons designated as authors qualify for authorship, and all those who qualify for authorship are listed.

Funding

The project was supported by NIH grant HL168874 (LFS) and the American Heart Association Postdoctoral Fellowship (https://doi.org/10.58275/AHA.25POST1378853.pc.gr.227467) (PR).

Acknowledgements

We thank Mr. Josh Tulman for original illustrations.

References

Balke CW, Egan TM & Wier WG. (1994). Processes that remove calcium from the cytoplasm during excitation-contraction coupling in intact rat heart cells. *J Physiol* **474,** 447-462.

Bertero E & Maack C. (2018). Calcium Signaling and Reactive Oxygen Species in Mitochondria. *Circ Res* **122,** 1460-1478.

Cannell MB, Cheng H & Lederer WJ. (1995). The control of calcium release in heart muscle. *Science* **268,** 1045-1049.

Cao Y, Vergnes L, Wang YC, Pan C, Chella Krishnan K, Moore TM, Rosa-Garrido M, Kimball TH, Zhou Z, Charugundla S, Rau CD, Seldin MM, Wang J, Wang Y, Vondriska TM, Reue K & Lusis AJ. (2022). Sex differences in heart mitochondria regulate diastolic dysfunction. *Nat Commun* **13,** 3850.

Chen W, London R, Murphy E & Steenbergen C. (1998). Regulation of the Ca2+ gradient across the sarcoplasmic reticulum in perfused rabbit heart. A 19F nuclear magnetic resonance study. *Circ Res* **83,** 898-907.

Chen Y, Csordas G, Jowdy C, Schneider TG, Csordas N, Wang W, Liu Y, Kohlhaas M, Meiser M, Bergem S, Nerbonne JM, Dorn GW, 2nd & Maack C. (2012). Mitofusin 2-containing mitochondrial-reticular microdomains direct rapid cardiomyocyte bioenergetic responses via interorganelle Ca(2+) crosstalk. *Circ Res* **111,** 863-875.

Cheng H, Lederer WJ & Cannell MB. (1993). Calcium sparks: elementary events underlying excitation-contraction coupling in heart muscle. *Science* **262,** 740-744.

Clements RT, Terentyeva R, Hamilton S, Janssen PML, Roder K, Martin BY, Perger F, Schneider T, Nichtova Z, Das AS, Veress R, Lee BS, Kim DG, Koren G, Stratton MS, Csordas G, Accornero F, Belevych AE, Gyorke S & Terentyev D. (2023). Sexual dimorphism in bidirectional SR-mitochondria crosstalk in ventricular cardiomyocytes. *Basic Res Cardiol* **118,** 15.

Denton RM & McCormack JG. (1990). Ca2+ as a second messenger within mitochondria of the heart and other tissues. *Annu Rev Physiol* **52,** 451-466.

Denton RM, McCormack JG & Edgell NJ. (1980). Role of calcium ions in the regulation of intramitochondrial metabolism. Effects of Na+, Mg2+ and ruthenium red on the Ca2+-stimulated oxidation of oxoglutarate and on pyruvate dehydrogenase activity in intact rat heart mitochondria. *Biochem J* **190,** 107-117.

Dixon RE, Moreno CM, Yuan C, Opitz-Araya X, Binder MD, Navedo MF & Santana LF. (2015). Graded Ca(2)(+)/calmodulin-dependent coupling of voltage-gated CaV1.2 channels. *Elife* **4**.

Dixon RE, Yuan C, Cheng EP, Navedo MF & Santana LF. (2012). Ca2+ signaling amplification by oligomerization of L-type Cav1.2 channels. *Proc Natl Acad Sci U S A* **109,** 1749-1754.

Dorn GW, 2nd, Song M & Walsh K. (2015). Functional implications of mitofusin 2-mediated mitochondrial-SR tethering. *J Mol Cell Cardiol* **78,** 123-128.

Eisner D & Murphy E. (2024). Honey, they shrunk the ATP. *Proc Natl Acad Sci U S A* **121,** e2410446121.

Eisner DA, Caldwell JL, Kistamas K & Trafford AW. (2017). Calcium and Excitation-Contraction Coupling in the Heart. *Circ Res* **121,** 181-195.

Fabiato A. (1983). Calcium-induced release of calcium from the cardiac sarcoplasmic reticulum. *Am J Physiol* **245,** C1-14.

Feigl EO. (1983). Coronary physiology. *Physiol Rev* **63,** 1-205.

Garbincius JF & Elrod JW. (2022). Mitochondrial calcium exchange in physiology and disease. *Physiol Rev* **102,** 893-992.

Hom J & Sheu SS. (2009). Morphological dynamics of mitochondria--a special emphasis on cardiac muscle cells. *J Mol Cell Cardiol* **46,** 811-820.

Kirichok Y, Krapivinsky G & Clapham DE. (2004). The mitochondrial calcium uniporter is a highly selective ion channel. *Nature* **427,** 360-364.

Li L, Chu G, Kranias EG & Bers DM. (1998). Cardiac myocyte calcium transport in phospholamban knockout mouse: relaxation and endogenous CaMKII effects. *Am J Physiol* **274,** H1335-1347.

Lobas MA, Tao R, Nagai J, Kronschlager MT, Borden PM, Marvin JS, Looger LL & Khakh BS. (2019). A genetically encoded single-wavelength sensor for imaging cytosolic and cell surface ATP. *Nat Commun* **10,** 711.

Lopaschuk GD, Karwi QG, Tian R, Wende AR & Abel ED. (2021). Cardiac Energy Metabolism in Heart Failure. *Circ Res* **128,** 1487-1513.

López-López JR, Shacklock PS, Balke CW & Wier WG. (1995). Local calcium transients triggered by single L-type calcium channel currents in cardiac cells. *Science* **268,** 1042-1045.

Manning D, Rivera EJ & Santana LF. (2024). The life cycle of a capillary: Mechanisms of angiogenesis and rarefaction in microvascular physiology and pathologies. *Vascul Pharmacol* **156,** 107393.

Marvin JS, Kokotos AC, Kumar M, Pulido C, Tkachuk AN, Yao JS, Brown TA & Ryan TA. (2024). iATPSnFR2: A high-dynamic-range fluorescent sensor for monitoring intracellular ATP. *Proc Natl Acad Sci U S A* **121,** e2314604121.

McCormack JG, Halestrap AP & Denton RM. (1990). Role of calcium ions in regulation of mammalian intramitochondrial metabolism. *Physiol Rev* **70,** 391-425.

Moreland JE. (1962). Electron microscopic studies of mitochondria in cardiac and skeletal muscle from hibernated ground squirrels. *Anat Rec* **142,** 155-167.

Murphy E & Steenbergen C. (2008). Ion transport and energetics during cell death and protection. *Physiology (Bethesda)* **23,** 115-123.

Rangaraju V, Calloway N & Ryan TA. (2014). Activity-driven local ATP synthesis is required for synaptic function. *Cell* **156,** 825-835.

Rhana P, Matsumoto C, Fong Z, Costa AD, Del Villar SG, Dixon RE & Santana LF. (2024). Fueling the heartbeat: Dynamic regulation of intracellular ATP during excitation-contraction coupling in ventricular myocytes. *Proc Natl Acad Sci U S A* **121,** e2318535121.

Rossow CF, Dilly KW, Yuan C, Nieves-Cintron M, Cabarrus JL & Santana LF. (2009). NFATc3-dependent loss of I(to) gradient across the left ventricular wall during chronic beta adrenergic stimulation. *J Mol Cell Cardiol* **46,** 249-256.

Saddik M & Lopaschuk GD. (1991). Myocardial triglyceride turnover and contribution to energy substrate utilization in isolated working rat hearts. *J Biol Chem* **266,** 8162-8170.

Santana LF, Cheng H, Gomez AM, Cannell MB & Lederer WJ. (1996). Relation between the sarcolemmal Ca2+ current and Ca2+ sparks and local control theories for cardiac excitation-contraction coupling. *Circ Res* **78,** 166-171.

Schwenke WD, Soboll S, Seitz HJ & Sies H. (1981). Mitochondrial and cytosolic ATP/ADP ratios in rat liver in vivo. *Biochem J* **200,** 405-408.

Shioya T. (2007). A Simple Technique for Isolating Healthy Heart Cells from Mouse Models. *The Journal of Physiological Sciences* **57,** 327-335.

Spooner HC, Costa AD, Westhoff M, Hernandez-Gonzalez A, Ibrahimkhail H, Yarov-Yarovoy V, Horne MC, Dickson EJ & Dixon RE. (2025). 14-3-3 promotes sarcolemmal expression of cardiac Ca(V)1.2 and nucleates isoproterenol-triggered channel superclustering. *Proc Natl Acad Sci U S A* **122,** e2413308122.

Wang SQ, Song LS, Lakatta EG & Cheng H. (2001). Ca2+ signalling between single L-type Ca2+ channels and ryanodine receptors in heart cells. *Nature* **410,** 592-596.

Westhoff M, Del Villar SG, Voelker TL, Thai PN, Spooner HC, Costa AD, Sirish P, Chiamvimonvat N, Dickson EJ & Dixon RE. (2024). BIN1 knockdown rescues systolic dysfunction in aging male mouse hearts. *Nat Commun* **15,** 3528.

Wisneski JA, Stanley WC, Neese RA & Gertz EW. (1990). Effects of acute hyperglycemia on myocardial glycolytic activity in humans. *J Clin Invest* **85,** 1648-1656.

Yaniv Y, Spurgeon HA, Ziman BD, Lyashkov AE & Lakatta EG. (2013). Mechanisms that match ATP supply to demand in cardiac pacemaker cells during high ATP demand. *Am J Physiol Heart Circ Physiol* **304,** H1428-1438.

Zhou B & Tian R. (2018). Mitochondrial dysfunction in pathophysiology of heart failure. *J Clin Invest* **128,** 3716-3726.

Figures

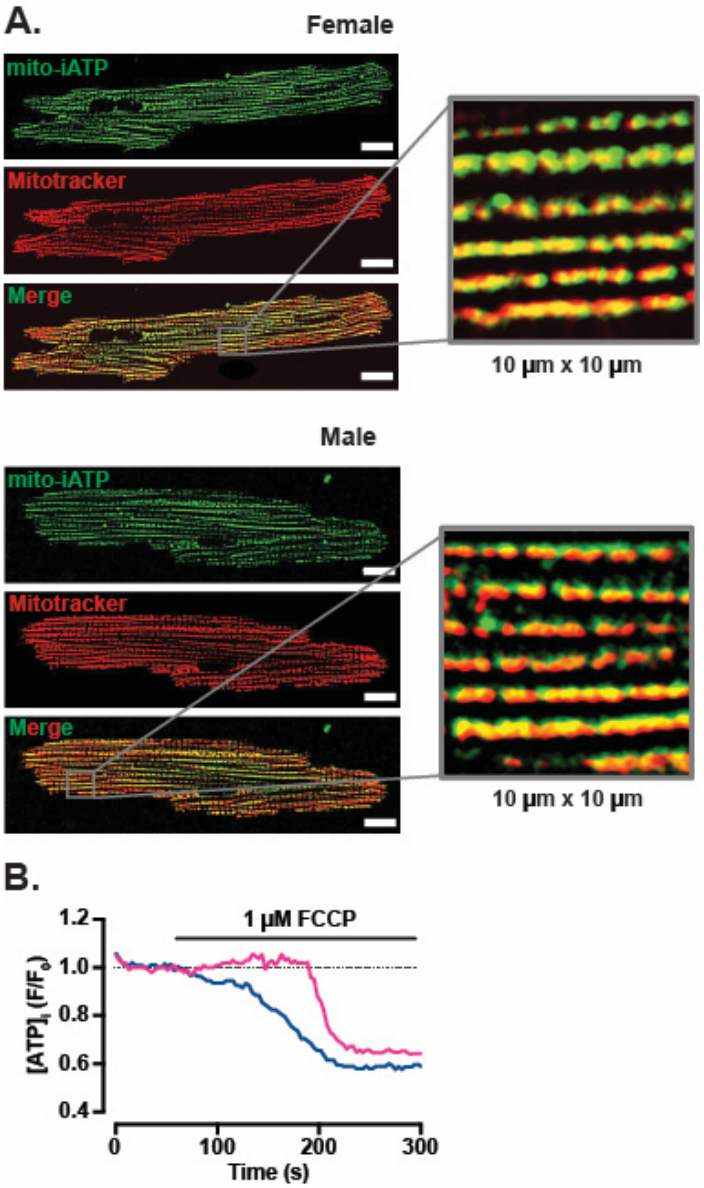

Figure 1. Targeting and validation of the mitochondrial ATP sensor, mito-iATP, in adult mouse ventricular myocytes. (A) Live-cell, wide-field confocal images of myocytes expressing mito-iATP (green) and Mitotracker Deep Red (red). The merged panel and 10 x 10 µm inset demonstrate pixel-level concordance between channels. Manders colocalization coefficient: female, 0.94 ± 0.005 (n = 19 myocytes); male, 0.99 ± 0.001 (n = 24 myocytes). Scale bars: 10 µm. (B) Sensitivity of the mitochondrial ATP sensor for ATP. Time course of normalized mito-iATP fluorescence (F/F_0), showing a decrease (~40%) in fluorescence after bath application of 1 µM FCCP ($P < 0.0001$, $n = 21$ cells).

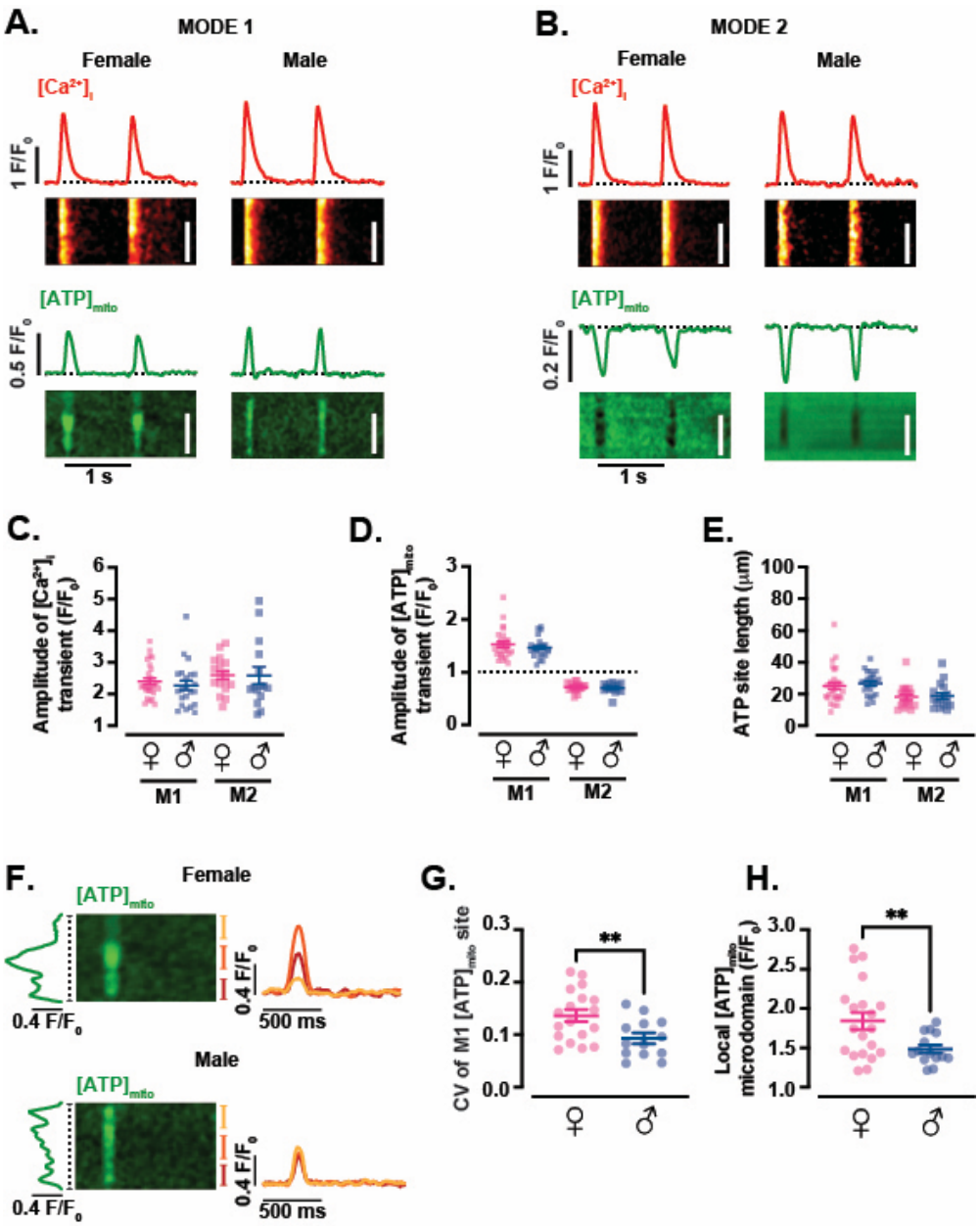

Figure 2. Beat-locked mitochondrial ATP transients adopt two discrete waveforms (Modes 1 and 2). (A, B) Representative line-scan images of $[Ca^{2+}]_i$ (top) and $[ATP]_{mito}$ (bottom) from female and male myocytes with Mode 1 (A) or Mode 2 (B) ATP dynamics. Red and green traces above each line-scan show $[Ca^{2+}]_i$ and $[ATP]_{mito}$ time courses, respectively. Scale bars: 20 μm. (C–E) Scatter plots of the amplitudes of $[Ca^{2+}]_i$ (C) and $[ATP]_{mito}$ (D) transients, and spatial spread of $[ATP]_{mito}$ (E) in female (magenta) and male (blue) myocytes (N = 3 mice, *n* = 27 cells of Mode 1 sites and 17 cells of Mode 2 sites in females, and N = 3 mice, *n* = 22 cells of Mode 1 sites and 15 cells of Modes 2 sites in males). (F) Representative regions of interest in Mode 1 $[ATP]_{mito}$ microdomains in female (top) and male (bottom) myocytes. Green trace (left): spatial profile of the $[ATP]_{mito}$ signal oriented along the dotted line. Red, yellow, and orange traces: normalized fluorescence intensity of the local $[ATP]_{mito}$ microdomain. (G, H) Scatter plots of the coefficient of variation (CV) of Mode 1 $[ATP]_{mito}$ sites (G) and peak amplitude for the $[ATP]_{mito}$ microdomain (H).

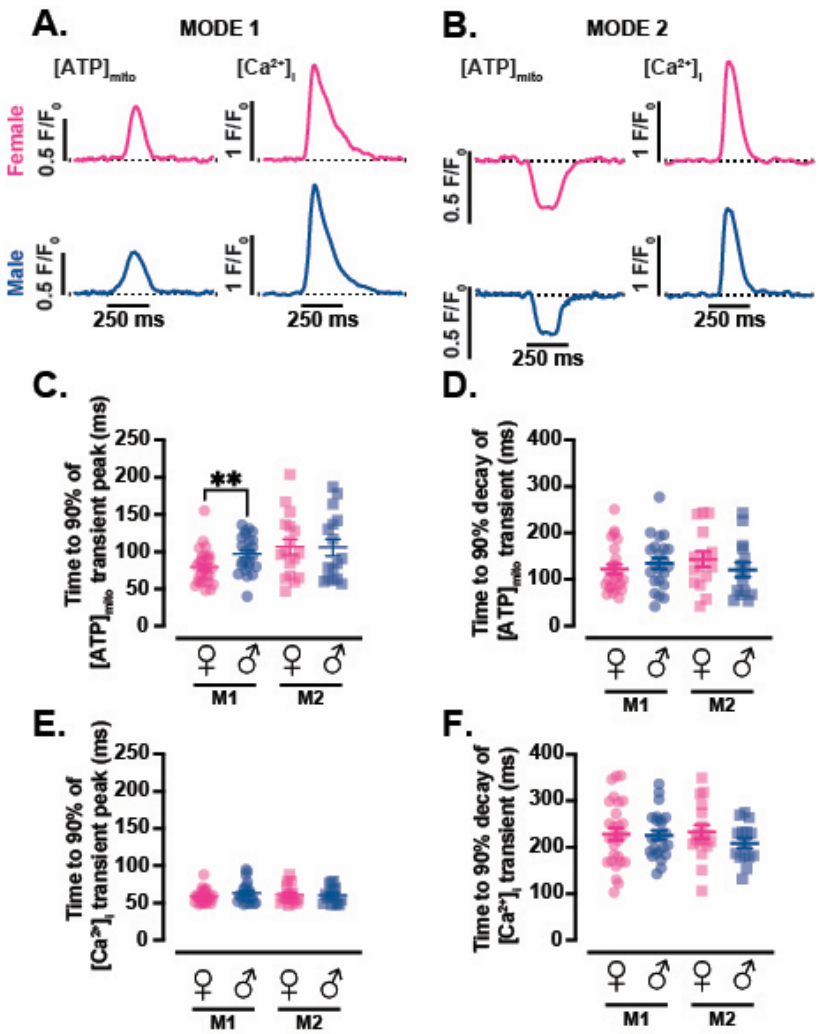

Figure 3. Action potential-induced mitochondrial ATP transients exhibit mode- and sex-dependent kinetic differences. (A, B) Time course of Mode 1 (A) and Mode 2 (B) $[ATP]_{mito}$ and $[Ca^{2+}]_i$ transients from female (magenta) and male (blue) myocytes. (C, D) Scatter plots for time to 90% of the $[ATP]_{mito}$ transient peak (C) and decay (D) in Mode 1 and Mode 2 regions of female (magenta) and male (blue) myocytes. (E, F) Scatter plots for time to 90% of the $[Ca^{2+}]_i$ transient peak (E) and decay (F) in Mode 1 and Mode 2 regions of female and male myocytes. Data are presented as means ± SEM (N = 3 mice, *n* = 27 cells of Mode 1 sites and 17 of Mode 2 sites in females, and N = 3 mice, *n* = 22 cells of Mode 1 sites and 15 cells of Mode 2 sites in males; $P < 0.05$, Student's *t*-test).

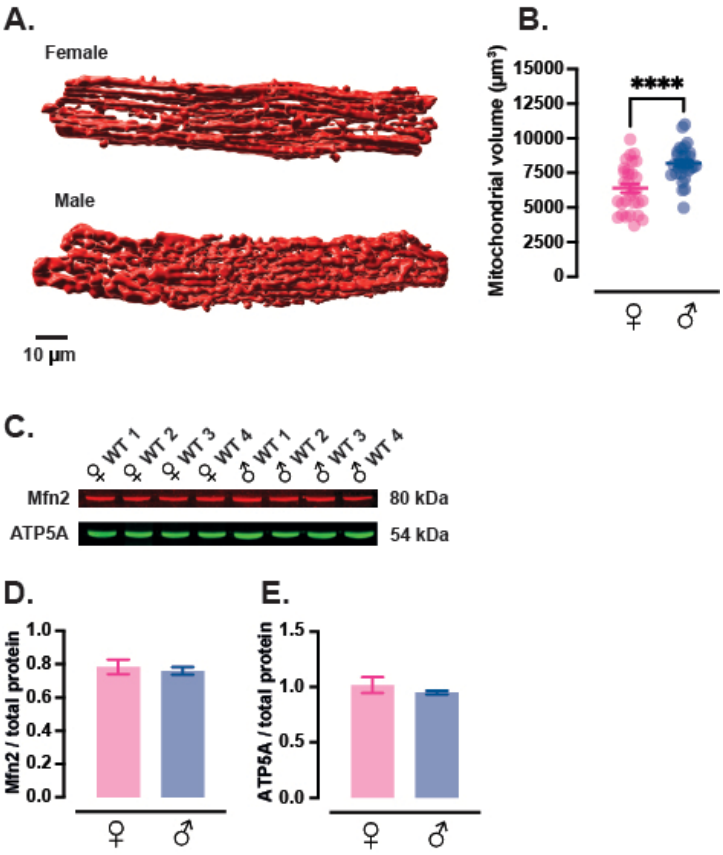

Figure 4. Female myocytes harbor a smaller mitochondrial volume but exhibit tighter SR–mitochondrial coupling. (A) 3D reconstructions of the mitochondrial volume in a female (top) and male (bottom) ventricular myocyte. Mitochondria were volumetrically rendered from deconvolved confocal z-stacks after staining with MitoTracker Deep Red. (B) Scatter plot of the mitochondrial volume in female (magenta) and male (blue) myocytes. (C) Representative immunoblots of the mitochondrial outer-membrane tether protein Mfn2 (80 kDa) and ATP5A (54 kDa) in ventricular lysates from four female (♀ WT 1–4) and four male (♂ WT 1–4) mice. Total protein stain served as loading control. (D, E) Densitometric quantification of Mfn2 (D) and ATP5A (E), normalized to total protein. Data are presented as means ± SEM (error bars; N = 4 mice).

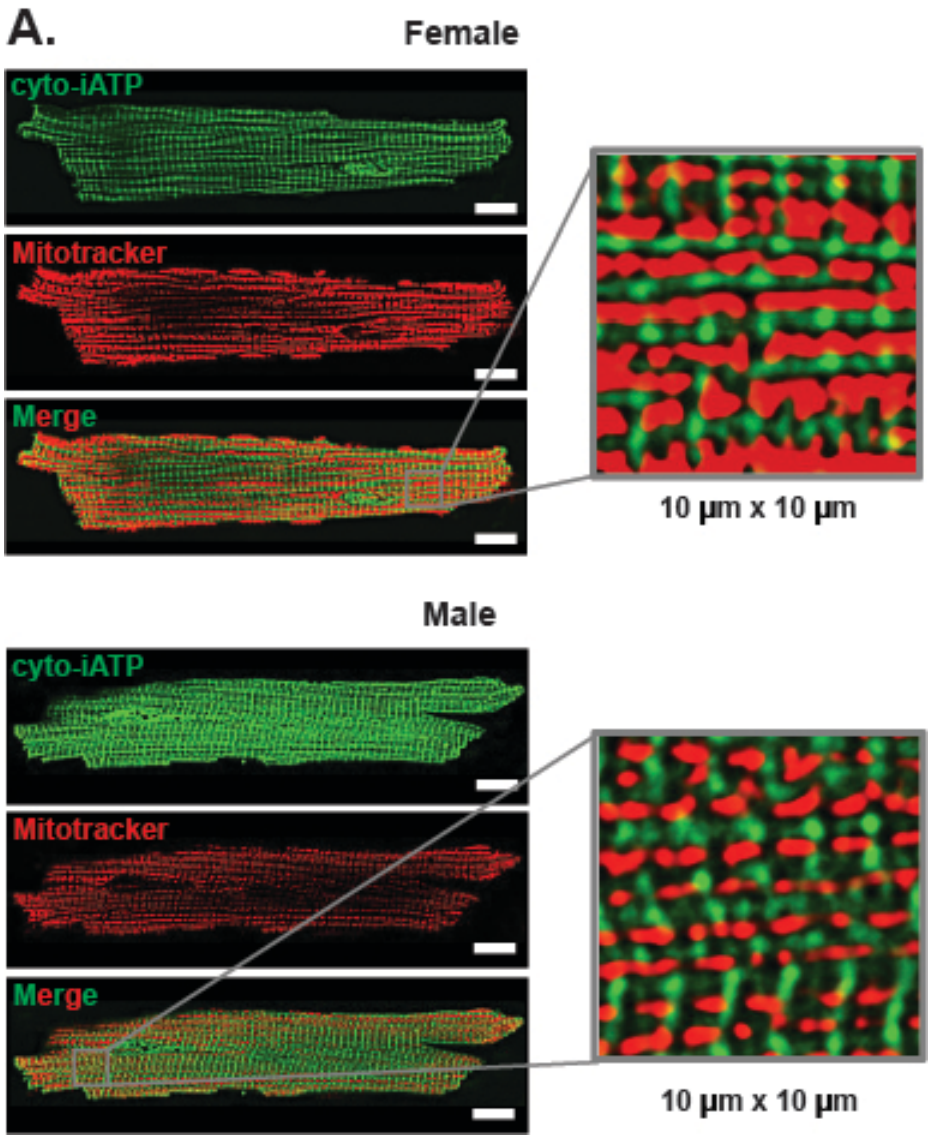

Figure 5. Cyto-iATP is excluded from mitochondria. Live-cell, wide-field confocal images of female (top) and male (bottom) ventricular myocytes expressing cyto-iATP (green) and Mitotracker Deep Red (red). The merged panel and 10 x 10 µm inset demonstrate minimal pixel-level overlap between channels. Manders colocalization coefficient: females, 0.68 ± 0.02 (n = 31 myocytes); males, 0.57 ± 0.02 (n = 34 myocytes). Scale bars: 10 µm.

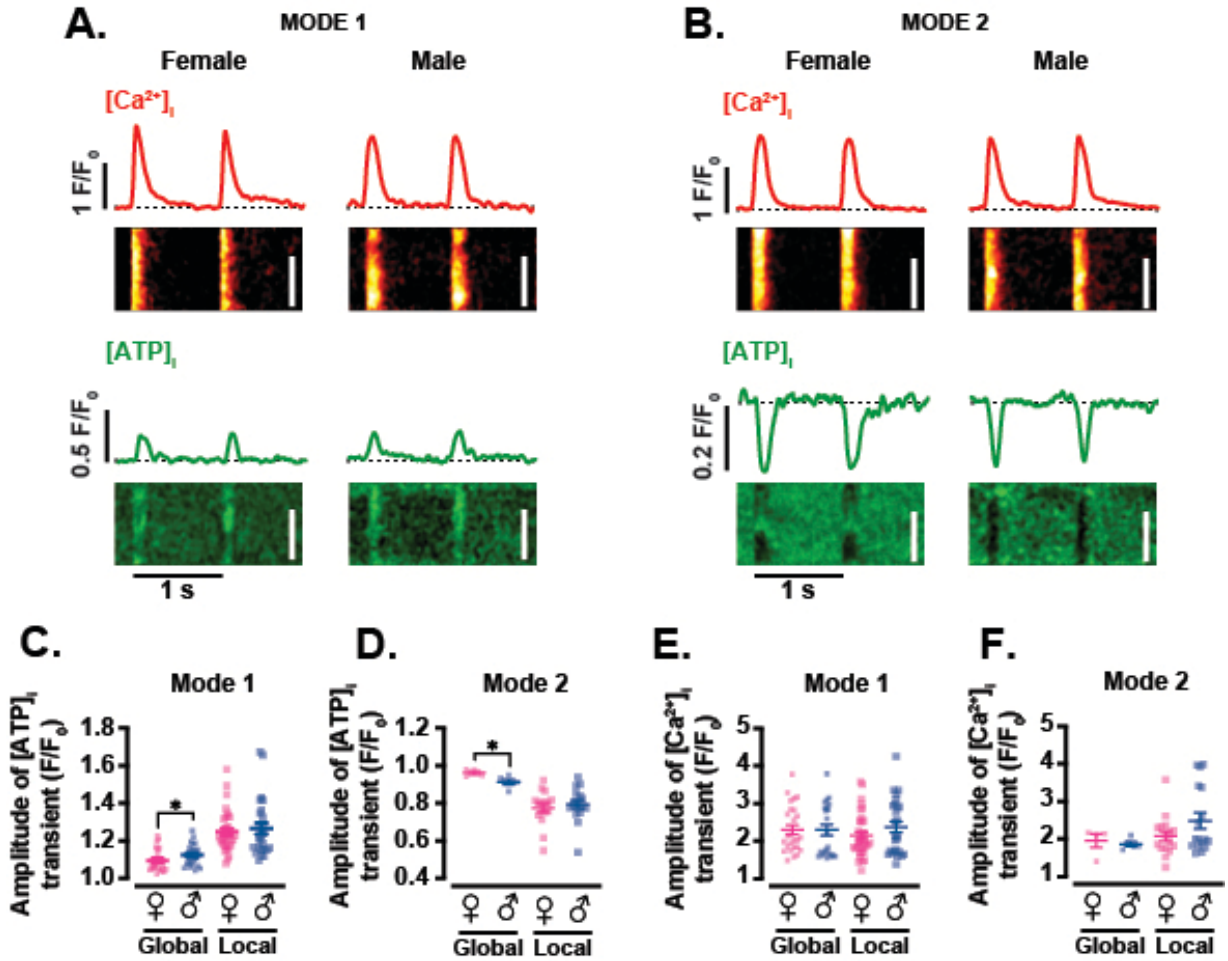

Figure 6. Cytosolic ATP transients mirror mitochondrial modes and show sex-dependent domain organization. (A, B) Representative line-scan images of $[Ca^{2+}]_i$ (top) and $[ATP]_i$ (bottom) in female and male myocytes with Mode 1 (A) or Mode 2 (B) ATP dynamics. Red and green traces above each line-scan show the time course of $[Ca^{2+}]_i$ and $[ATP]_i$ transients, respectively. Scale bars: 20 µm. (C, D) Scatter plots of global and local amplitudes of $[ATP]_i$ transients in Mode 1 (C) and Mode 2 (D) sites in female (magenta) and male (blue) myocytes. (E, F) Scatter plots of global and local amplitudes of $[Ca^{2+}]_i$ transients in Mode 1 (E) and Mode 2 (F) sites in female and male myocytes. (N = 4 mice, *n* = 35 cells of Mode 1 sites and 16 cells of Mode 2 sites in females, and N = 3 mice, *n* = 26 cells of Mode 1 sites and 17 cells of Mode 2 sites in males).

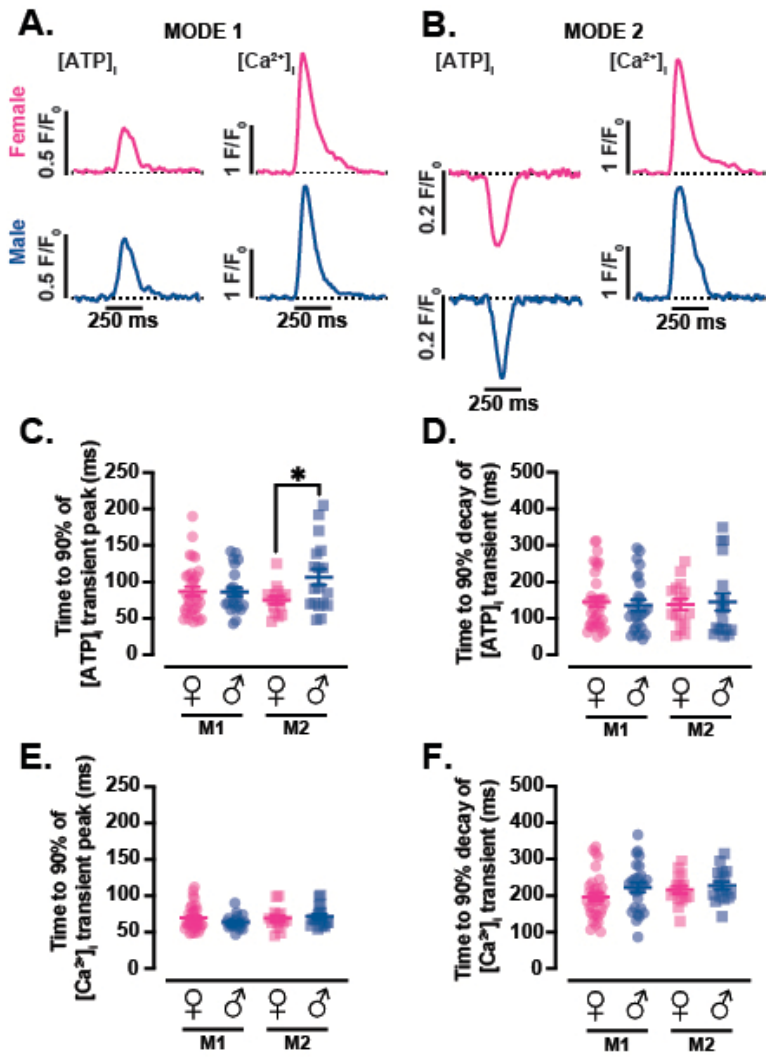

Figure 7. Kinetics of action potential-induced cytosolic ATP transients differ by mode but not by sex. (A, B) Time course of Mode 1 (A) and Mode 2 (B) $[ATP]_i$ and $[Ca^{2+}]_i$ transients in female (magenta) and male (blue) myocytes. (C, D) Scatter plots for time to 90% of $[ATP]_i$ transient peak (C) and decay (D) in Mode 1 and Mode 2 regions of female (magenta) and male (blue) myocytes. (E, F) Scatter plots for time to 90% of $[Ca^{2+}]_i$ transient peak (E) and decay (F) in Mode 1 and Mode 2 regions of female and male myocytes. Data are presented as means ± SEM (N = 4 mice, *n* = 34 cells of Mode 1 sites and 15 cells of Mode 2 sites in females, and N = 3 mice, *n* = 24 cells of Mode 1 sites and 18 cells of Mode 2 site in males; $P < 0.05$, Student's *t*-test).

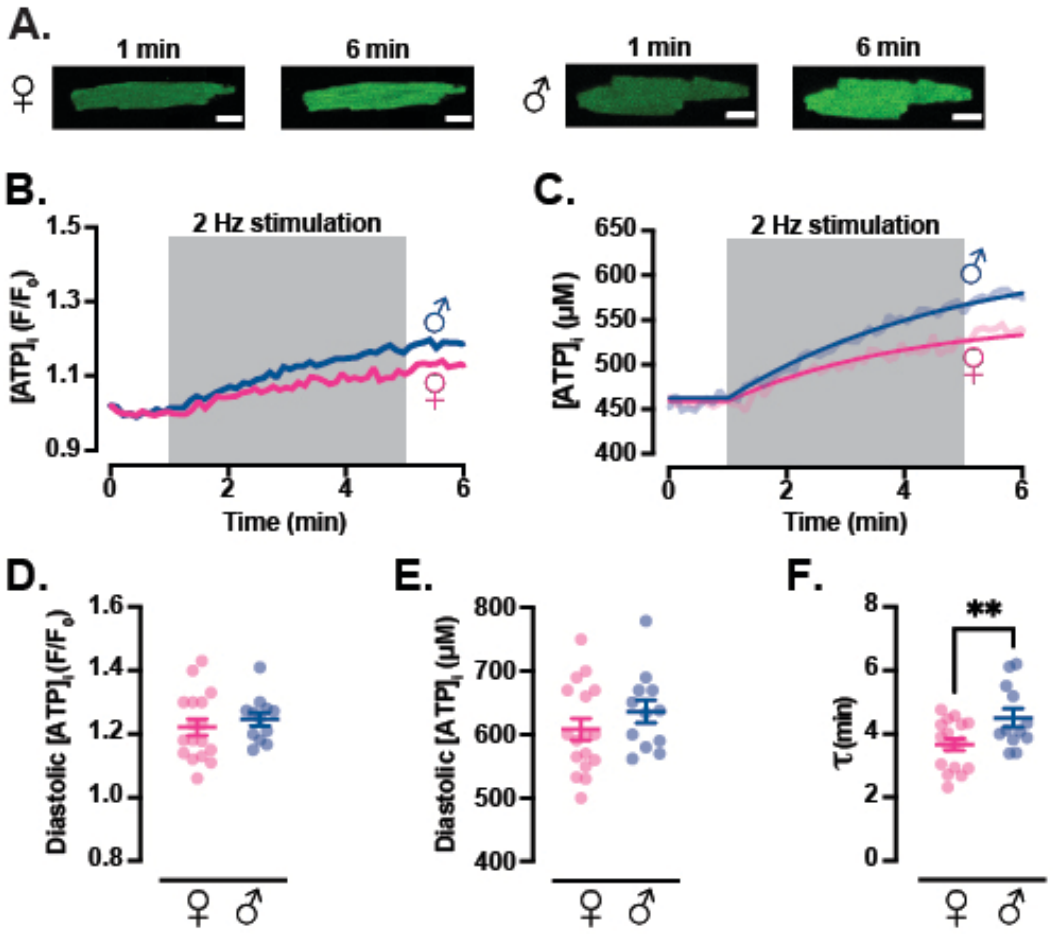

Figure 8. Diastolic cytosolic ATP rises with increased pacing frequency. (A) Representative confocal images of female (♀, left) and male (♂, right) ventricular myocytes expressing cyto-iATP. Fluorescence is shown before (1 minute) and after (6 minutes) 2 Hz field stimulation. Scale bars, 10 μm. (B) Representative time course of $[ATP]_i$ fluorescence (F/F_0) during the 6-minute experiment in female (magenta) and (male) myocytes. The gray box indicates the 2-Hz stimulation period (1–5 minutes). F/F_0 data were converted to intracellular ATP concentration (μM) using a pseudo-ratiometric method. (D, E) Scatter plots of diastolic $[ATP]_i$ at the end of 2 Hz stimulation, expressed as normalized fluorescence (D) and as concentration (μM) (E). (F) Scatter plot of the time constant for the rise in $[ATP]_i$ during pacing. Data are expressed as means ± SEM (females, *n* = 17 myocytes from 3 mice; males, *n* = 12 myocytes from 3 mice).

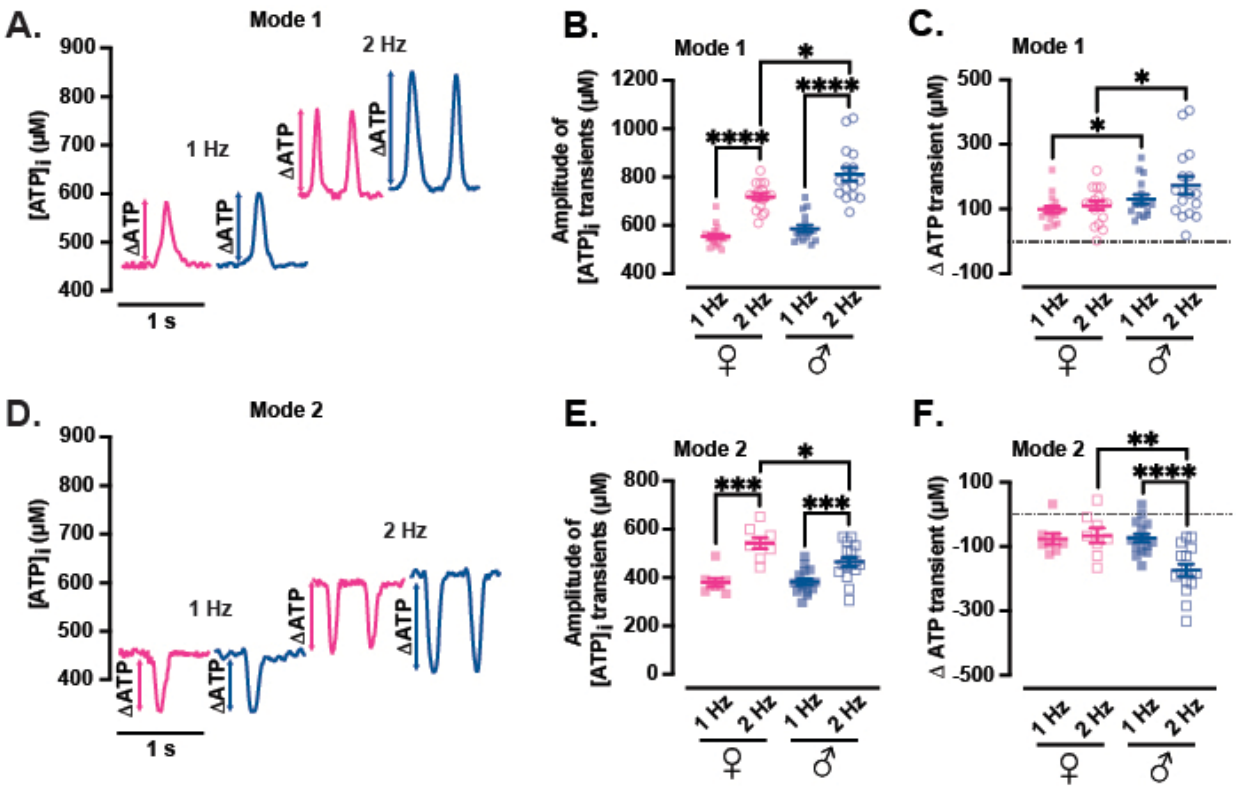

Figure 9. Increased workload amplifies cytosolic ATP transients in male but not female myocytes. (A) Representatives time course of $[ATP]_i$ from female (magenta) and male (blue) Mode 1 myocytes field-stimulated at 1 Hz (left) or 2 Hz (right). Double-headed arrows indicate the net shift in $[ATP]_i$ consumption or production (ΔATP) after increasing workload (2 Hz). (B, C) Scatter plots of the amplitudes of Mode 1 myocyte $[ATP]_i$ transients (B) and ΔATP transients (C). (D) Representatives time course of $[ATP]_i$ from female (magenta) and male (blue) Mode 2 myocytes field-stimulated at 1 Hz (left) or 2 Hz (right). Double-headed arrows indicate the net shift in $[ATP]_i$ consumption or production (ΔATP) after increasing workload (2 Hz). (E, F) Scatter plots of the amplitudes of Mode 2 myocyte $[ATP]_i$ transients (E) and ΔATP transients (F). Data are presented as means ± SEM (N = 3 mice, *n* = 17 cells of Mode 1 sites and 8 cells of Mode 2 sites in females, and N = 3 mice, *n* = 16 cells of Mode 1 sites and 16 cells of Mode 2 sites in males).

Abstract figure

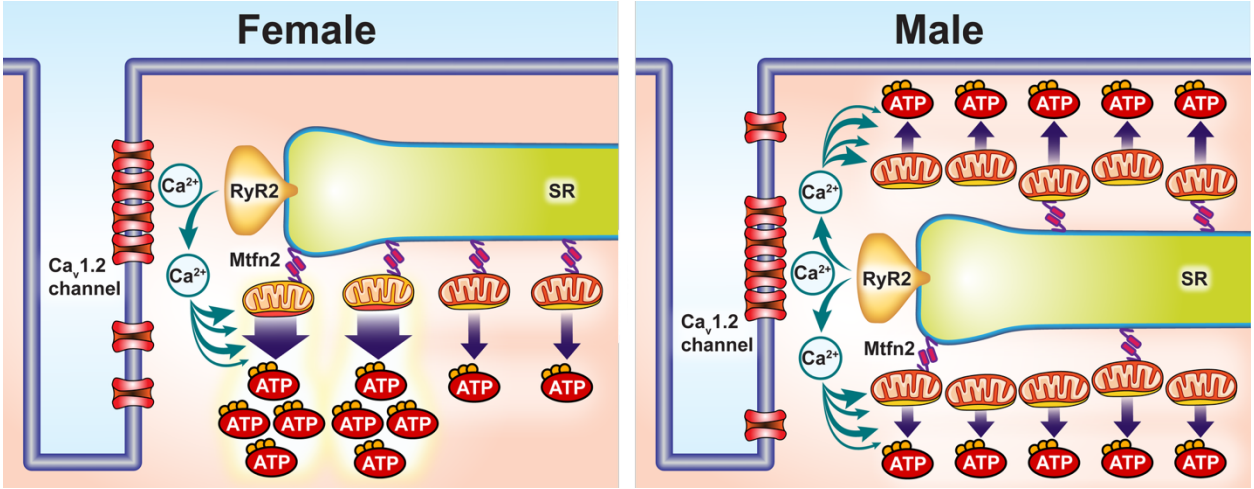

Legend: Excitation of ventricular myocytes triggers Ca^{2+} entry through T-tubular L-type $Ca_V1.2$ channels (red), activating type-2 ryanodine receptor (RyR2) clusters in the adjoining sarcoplasmic reticulum (SR). Released Ca^{2+} traverses the 12-nm cleft and enters subsarcolemmal mitochondria via mitofusin-2 (Mfn2) tethers (magenta), accelerating oxidative phosphorylation to generate ATP (red ovals). In female myocytes (left), a select subset of tightly SR-coupled mitochondria produces large, beat-locked ATP surges that create localized energetic micro-domains. In male myocytes (right), looser SR–mitochondrial spacing and a greater mitochondrial density distribute the Ca^{2+} load evenly, yielding smaller but spatially uniform ATP transients. Thus, sex-specific differences in SR–mitochondrial nano coupling—not the excitation–contraction sequence itself—determine the amplitude and heterogeneity of beat-to-beat ATP supply in the heart.